Supporting information

The unique evolution of transport bands and thermoelectric performance enhancement by extending low-symmetry phase to high temperature in tin selenide

Kunling Peng[‖a], Bo Zhang[‖b], Hong Wu[c], Hailiang Che[a], Xuefeng Sun[a], Jianjun Ying[a], Zhe Sun[b], Guoyu Wang[d], Xiaoyuan Zhou*[c], Xianhui Chen*[a].

[a] Department of Physics and Hefei National Laboratory for Physical Science at Microscale, University of Science and Technology of China, Hefei, Anhui 230026, People's Republic of China

[b] National Synchrotron Radiation Laboratory, University of Science and Technology of China, Hefei, Anhui 230029, People's Republic of China

[c] College of Physics, Chongqing University, Chongqing 401331, People's Republic of China

[d] Chongqing Institute of Green and Intelligent Technology, Chinese Academy of Sciences, Chongqing 400714, People's Republic of China.

E-mail: chenxh@ustc.edu.cn; xiaoyuan2013@cqu.edu.cn

Experimental and theoretical methods

Synthesis

Elemental constituents are weighed according to the stoichiometry, and loaded into cone-shaped silica tubes under argon atmosphere and sealed at 5×10^{-4} Pa. Then the cone-shaped silica tube is placed inside another large silica tube, again evacuated and flame-sealed, which aims at protecting the crystal from oxidation because the cone-shaped silica tubes is vulnerable as the crystal structure undergoes a phase transition from the Cmcm to Pnma phase. Single crystals are grown by a modified Bridgeman method. Excellent single crystalline ingots of SnSe and $SnSe_{0.7}S_{0.3}$ with the diameter of 13 mm and the height of 40 mm are obtained

Thermoelectric transport property measurement

The direction of obtained single crystal ingots are studied by Laue diffraction. The single crystal ingots are cut into bars with dimensions ~ 8 mm × 2.5 mm × 2.5 mm for electrical property measurements, and square planar samples of ~ 6 mm × 6 mm × 1.5 mm for thermal conductivity measurements along different directions (a-, b- and c-axis). The Seebeck coefficient S and electrical conductivity σ were measured on a commercial system (LSR-3, Linseis) under a static helium atmosphere. The high temperature (> 300 K) Hall coefficient (R_H) are measured using a home-made apparatus with the applied field of ±1 T. The Hall carrier density (n_H) is calculated by $1/eR_H$, where e is the elementary charge. Then the Hall mobility is calculated according to the equation $\sigma = en_H\mu_H$. The thermal conductivity is calculated from $\kappa = \rho D C_p$, where ρ, D and C_p are the density of samples, thermal diffusivity and specific heat capacity, respectively. The densities (~6.15 g/cm³

for SnSe and ~5.94 g/cm^3 for SnSe$_{0.7}$S$_{0.3}$) of samples are measured by Archimedes method on a commercial instrument (BR-120N, Beyongtest). The thermal diffusivity (D) is obtained on a LFA 457 (Netzsch) instrument with a flowing argon atmosphere. The specific heat capacity (C_p) is obtained by PPMS DynaCool-9T with HC module with the range from 2 K – 300 K, while but the liner relationship ($C_p = 0.26 + 10^{-4}(T - 300)/5$ for SnSe; $C_p = 0.275 + 10^{-4}(T - 300)/5$) is used for higher temperature. We estimated that the combined uncertainly for all measurements involved in the calculation of zT is around 15%. The lattice thermal conductivity (κ_l) is obtained by $\kappa_l = \kappa - \kappa_e$, and the κ_e is proportional to the electrical conductivity (σ) using the Wiedemann-Franz relation, $\kappa_e = L\sigma T$, where L is the Lorenz number. The heat flow is obtained on TA instrument SDT Q600. SEM and EDS analysis are obtained on ZEISS EVD MA10.

Density function theory (DFT) calculations

The projector augmented plane wave (PAW)[1,2] methods as implemented in the Vienna ab initio simulation package (VASP)[3] code is used for structure relaxation. The exchange-correlation functional is defined using a generalized gradient approximation (GGA) of Perdew-Burke-Ernzerhof (PBE)[4]. The total energies are numerically converged to 1×10^{-6} eV using a kinetic energy cutoff of 500 eV. For the Brillouin zone integrations, we use the Monkhorst-Park k-mesh scheme with $5 \times 9 \times 9$ for the primitive cell (Pnma, 8 atoms). The phonon band structure is determined by the density functional perturbation theory as implemented in VASP code and Phonopy program[5]. Lattice thermal conductivity is calculated by solving the linearized phonon Boltzmann equation and implemented by VASP and Phono3py code[6].

The DFT band structure are shown in Figure 3a-3c and Figure S7. The information (position, effective mass, degeneracy) for the top of valence band for each crystal is included in Table S5 and S6. The inertial effective mass tensor is defined as:

$$\frac{1}{m_{ij}^*} = \frac{1}{\hbar^2}\frac{\partial^2 E_n(\vec{k})}{\partial k_i k_j}, i,j = x,y,z \tag{S1}$$

where x,y,z are the direction in the reciprocal Cartesian space $(2\pi/A)$, $E_n(\vec{k})$ is the dispersion relation for the n-th electronic band, $\hbar$ is the reduced Planck constant. m_{xx}^*, m_{yy}^* and m_{zz}^* are the inertial effective masses along the different principal axes of the constant energy ellipsoids. In our case with strong anisotropy, it is necessary to average the effective masses along different axes. The conductive effective mass is calculated via harmonic mean:

$$m_c^* = 3\left[\frac{1}{m_{xx}^*} + \frac{1}{m_{yy}^*} + \frac{1}{m_{zz}^*}\right]^{-1} \tag{S2}$$

And in general, the conductive effective mass is the average inertia effective mass (m_I^*).

The total DOS effective mass is defined as:

$$m_d^* = N_v^{2/3} m_b^* \tag{S3}$$

with band effective mass:

$$m_b^* = \sqrt[3]{m_{xx}^* m_{yy}^* m_{zz}^*} \tag{S4}$$

Angle-resolved photoemission spectroscopy (ARPES) measurements

ARPES experiments are performed at BL-13U of National Synchrotron Radiation Laboratory (NSRL) at Hefei, equipped with VG-Scienta R4000 electron analyzers. The angular resolution of the electron analyzer is 0.3 degrees and the overall instrumental energy resolution is better than 20 meV. The flat and shiny surfaces are obtained through in situ cleavage under a vacuum pressure that is better than 6×10^{-11} mbar at a temperature of 20 K. The Fermi level of the samples is referenced using polycrystalline gold that was evaporated onto the sample holder.
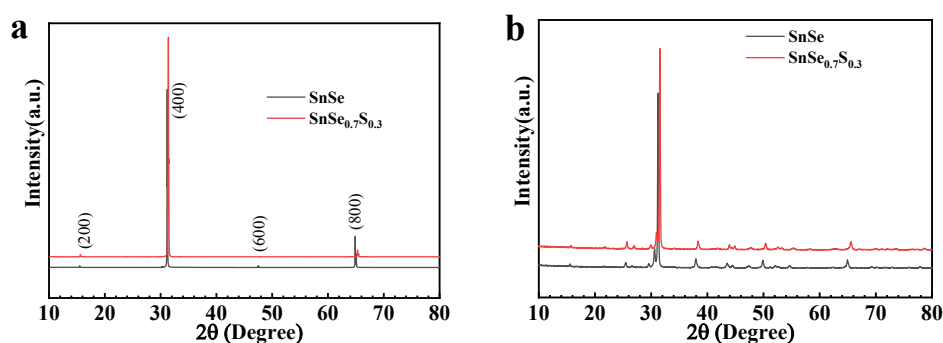
XRD

Figure S1. (a) XRD patterns of SnSe and $SnSe_{0.7}S_{0.3}$ along the cleavage plane and (b) powder XRD patterns.

Figure S1a displays the XRD patterns of SnSe and $SnSe_{0.7}S_{0.3}$ single crystals along the cleavage plane. The peak (200), (400), (600) and (800) can be recognized except for peak (600) of $SnSe_{0.7}S_{0.3}$ and confirm that the crystals are cleaved along the b-c plane. The as-prepared single crystals are crushed into powder and powder XRD patterns are carried out as shown in Figure S2b. The lattice parameters from the powder XRD patterns are shown in Table S1.

Table S1. Lattice parameters derived from the powder XRD patterns

Sample	a(Å)	b(Å)	c(Å)	Volume(Å^3)
SnSe	11.497±0.001	4.151±0.005	4.452±0.002	212.46
$SnSe_{0.7}S_{0.3}$	11.401±0.004	4.096±0.002	4.413±0.001	206.08

SEM-EDS
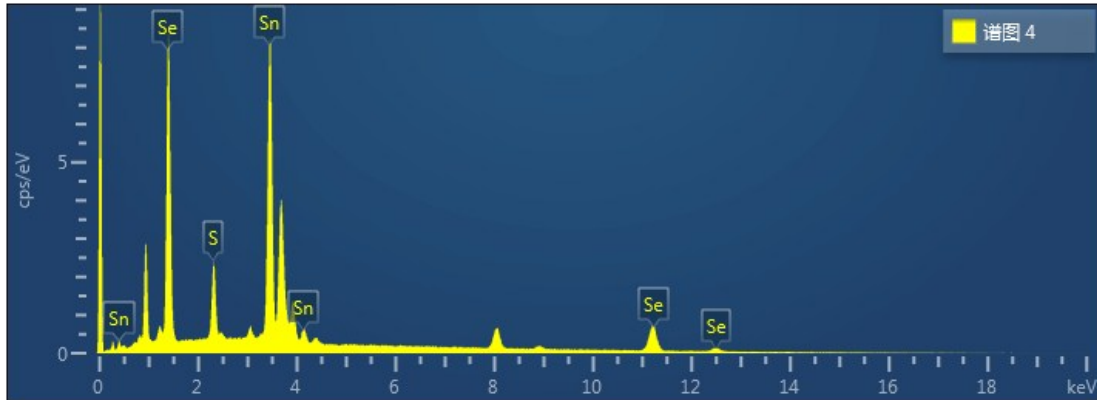
Figure S2. (a) SEM micrographs (1.5mm×1.0mm) with layered plot for a $SnSe_{0.7}S_{0.3}$ single crystal wafer. (b) EDS patterns for one position.

Results of SEM analyses (See Figure S2a) show surface morphology of $SnSe_{0.7}S_{0.3}$. The layered plot shows the homogeneous elemental distribution. EDS analyses shows composition (elemental distribution). We analyze three position on SEM micrographs as shown in figure S2a and atomic percent are presented on Table S2.

Table S2 Atomic percent of $SnSe_{0.7}S_{0.3}$ measured by EDS at different position as Figure S2a

Position	Sn (%)	Se (%)	S(%)	Total (%)
4	49.48	34.63	15.89	100
5	49.87	34.78	15.35	100
6	49.96	34.48	15.56	100

Lattice parameter
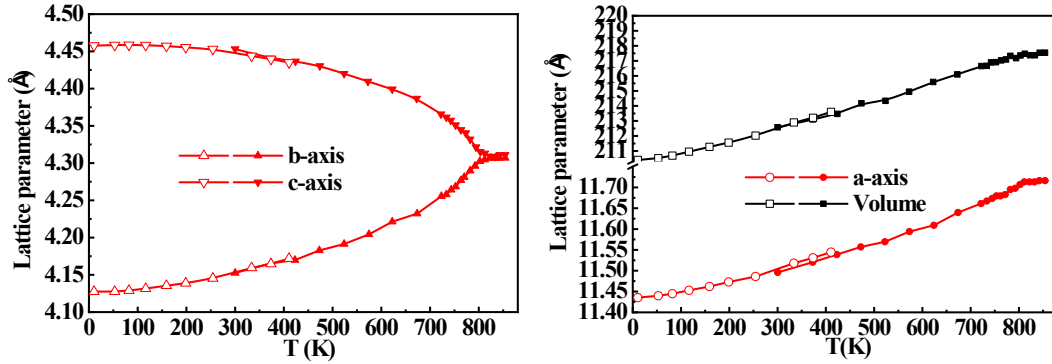

Figure S3. Temperature dependence lattice parameter of SnSe from previous reports[7, 8]. Vigorous lattice will affect the physical properties of the material.
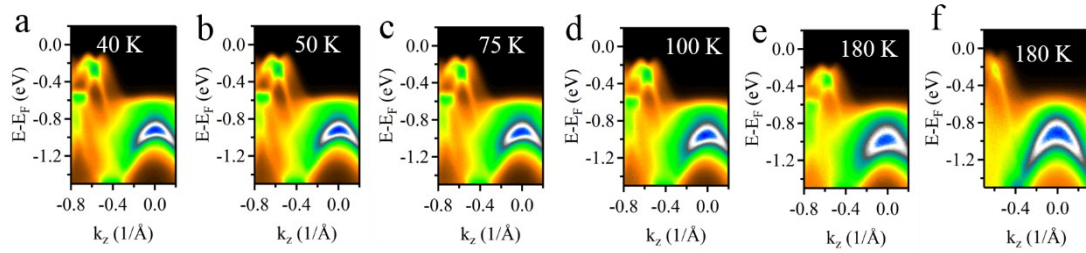
ARPES and band mass

Figure S4. The ARPES intensity plot of SnSe (a-e) and $SnSe_{0.7}S_{0.3}$ (f) along the Γ-Z directions at different temperatures.

Table S3 the band mass of SnSe from ARPES

T(K)	20	40	50	60	75	100	120	180	240	300
α_1	0.118	0.152	0.152	0.153	0.157	0.219	0.217	0.219	0.194	-
α_2	0.240	0.249	0.249	0.261	0.270	0.282	0.293	0.299	0.294	-

Table S4 the band mass of $SnSe_{0.7}S_{0.3}$ from ARPES

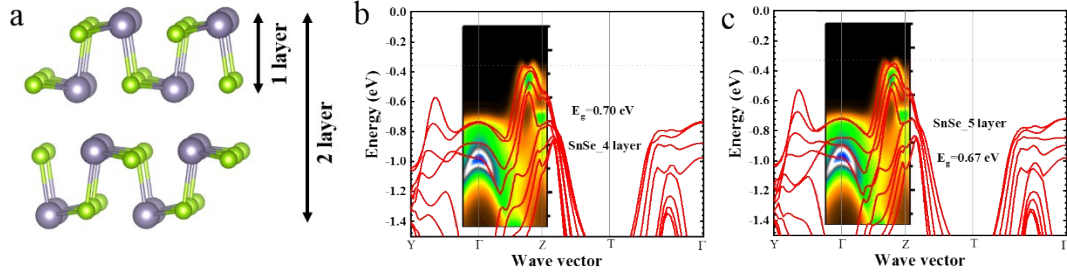| T(K)	20	60	120	180	240	300
α_1	0.158	0.159	0.174	0.182	0.197	0.194
α_2	0.171	0.172	0.239	0.256	0.251	0.243

ARPES and layered calculation

Figure S5. (a) Layer explanation. (b, c) band calculation with 4 and 5 layers respectively. The image under the data are the ARPES result of SnSe at 20 K.

Bulk and surface hold different electron wave functional and electron state, leading to the difference between bulk band structure and few layer band structure. Generally, for ARPES measurement, the wave function in the bulk will extend to the surface. So even if the electrons come out of the surface, the wave function carried by it still reflects the energy band of the bulk state. From Figure S6, the calculation band structure with 5 layer is similar to the ARPES results. The offset between the two extremums is about 10 meV which is less than our energy resolution of 20 meV. Furthermore, influenced by superposition state of electron wave function between bulk and surface, it is hardly find the highest extremum in ARPES measurements.
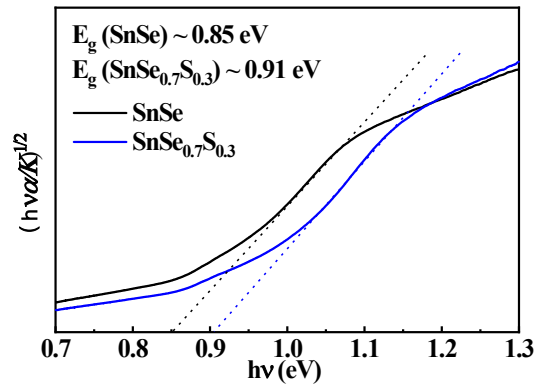
Infrared absorption spectrum

Figure S6. Infrared absorption spectrum at 300 K and band gap of the SnSe and $SnSe_{0.7}S_{0.3}$ single crystals. The band gap value of SnSe and $SnSe_{0.7}S_{0.3}$ measured in this work are 0.85 eV and 0.91 eV respectively.
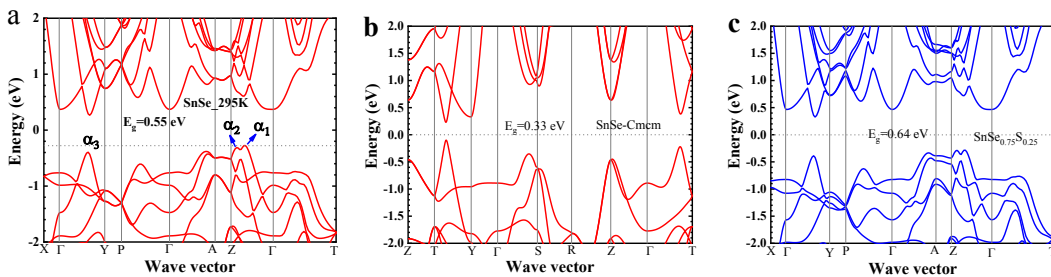
Band structure of SnSe and $SnSe_{0.75}S_{0.25}$

Figure S7. Electronic band structures of (a) low-temperature (Pnma), (b)high-temperature (Cmcm) phases of SnSe and (a) low-temperature (Pnma) of SnSe$_{0.75}$S$_{0.25}$.

Band structures of SnSe demonstrates that the gap of Pnma structure (~0.55 eV) is higher than gap of Cmcm structure (~0.33 eV) as shown in Figure S5. The calculation band gap of SnSe$_{0.75}$S$_{0.25}$ is 0.64 eV that larger than that of SnSe in Pnma structure. We also calculate the effective masses the two extremum valence bands of SnSe and SnSe$_{0.75}$S$_{0.25}$ along the Γ-Z directions as shown in Table S5.

Table S5. Effective masses obtained by fitting the band structure of SnSe and SnSe$_{0.75}$S$_{0.25}$ in Pnma structure.

Sample	Valence band tops	Extremum position ($\vec{k}$)	m^*_{kx} (m_e)	m^*_{ky} (m_e)	m^*_{kz} (m_e)	m^*_I (m_e)	m^*_b (m_e)	m^*_d (m_e) (N_v=2)
SnSe	α_1	(0, 0, 0.474)	0.162	0.360	0.759	0.292	0.354	0.562
SnSe	α_2	(0, 0, 0.609)	0.195	0.315	1.492	0.334	0.451	0.716
SnSe$_{0.75}$S$_{0.25}$	α_1	(0, 0, 0.47)	0.152	0.378	1.394	0.302	0.431	0.684
SnSe$_{0.75}$S$_{0.25}$	α_2	(0, 0, 0.61)	0.163	0.554	2.347	0.359	0.596	0.946

Table S6. Effective masses obtained by fitting the band structure of SnSe in Pnma structure at different temperature.

| Sample	Valence band tops	Extremum position ($\vec{k}$)	VBM (meV)	m^*_{kx} (m_e)	m^*_{ky} (m_e)	m^*_{kz} (m_e)	m^*_I (m_e)	m^*_b (m_e)	m^*_d (m_e) (N_v=2)
295 K	α_1	(0, 0, 0.474)	0	0.162	0.360	0.759	0.292	0.354	0.562
295 K	α_2	(0, 0, 0.609)	46	0.195	0.315	1.492	0.334	0.451	0.716
295 K	α_3	(0, 0.469, 0)	133	0.161	0.368	0.474	0.272	0.304	0.483
600 K	α_1	(0, 0, 0.501)	0	0.167	0.355	0.881	0.302	0.374	0.765
600 K	α_2	(0, 0, 0.615)	59	0.225	0.299	1.663	0.358	0.482	0.765
600 K	α_3	(0, 0.473, 0)	56	0.160	0.322	0.563	0.269	0.307	0.488
790 K	α_1	(0, 0, 0.522)	0	0.158	0.384	0.940	0.300	0.385	0.611
790 K	α_2	--	--	--	--	--	--	--	--
790 K	α_3	(0, 0.480, 0)	-52	0.145	0.278	0.731	0.253	0.309	0.490

Parabolic band model
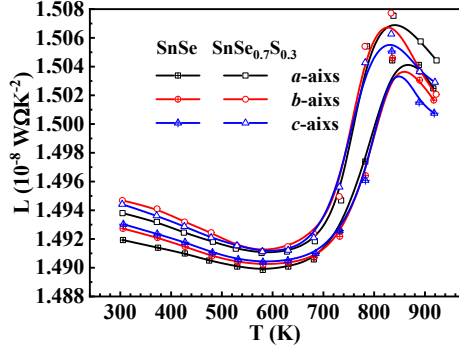
Figure S8. Lorenz number as a function of temperature for SnSe and SnSe$_{0.75}$S$_{0.25}$. The scattering factor (r) is -1/2.

The DOS effective mass and Lorenz number are calculated by single parabolic band model as following expression[9]:

$$m_d^* = \frac{1}{2k_B T}\left(\frac{h^3 p}{4\pi\, F_{\frac{1}{2}}(\eta_F)}\right)^{\frac{2}{3}}$$

(S5)

$$L = \left(\frac{k_B}{q}\right)^2\left[\frac{\left(r+\frac{7}{2}\right)F_{r+\frac{5}{2}}(\eta)}{\left(r+\frac{5}{2}\right)F_{r+\frac{1}{2}}(\eta)} - \left(\frac{\left(r+\frac{5}{2}\right)F_{r+\frac{3}{2}}(\eta)}{\left(r+\frac{3}{2}\right)F_{r+\frac{1}{2}}(\eta)}\right)^2\right]$$

(S6)

with the Fermi integral

$$F_n(\eta) = \int_0^\infty \frac{\xi^n}{1+e^{\xi-\eta}}d\xi$$

(S7)

where η is the reduced Fermi energy from the Seebeck coefficient given by equation (S4).

$$S = \pm\frac{k_B}{e}\left[\eta_F - \frac{\left(r+\frac{5}{2}\right)F_{r+\frac{3}{2}}(\eta_F)}{\left(r+\frac{3}{2}\right)F_{r+\frac{1}{2}}(\eta_F)}\right]$$

(S8)

The scattering factor (r) gives the exponent of the energy dependence on the carrier mean free path.

The DOS effective mass from single arabolic band model (SPB) at room temperature are 0.77 m$_e$ and 0.88 m$_e$ for SnSe and SnSe$_{0.7}$S$_{0.3}$ respectively. The carrier density is calculated by

$$p = \frac{4}{\sqrt{\pi}}\left(\frac{2\pi m_d^* k_B T}{h^2}\right)^{3/2}F_{\frac{1}{2}}(\eta_F)$$
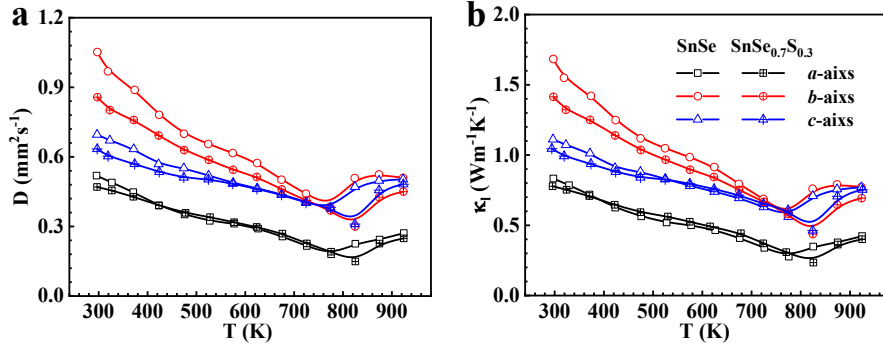
(S9)

Thermal transports

Figure S9. Thermal diffusivity and lattice thermal conductivity as a function of temperature along a-, b- and c-axis for SnSe and SnSe$_{0.75}$S$_{0.25}$.

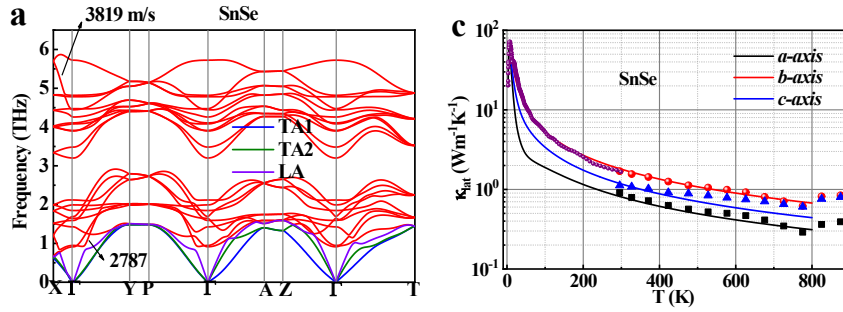## Phonon spectrum and DFT calculated κ_l

Figure S10. Theoretically calculated (a) phonon dispersion and (b) lattice thermal conductivity along different directions for SnSe.

Figure S10a shows phonon spectrum of SnSe. The highest frequency of the acoustic branch and optical mode are close to 1.6 THz and 6 THz respectively. Figure S8b shows the experimental and theoretical calculated the lattice thermal conductivity of SnSe. Here, we only consider the three-phonon umklapp process for calculation lattice thermal conductivity and calculate Pnma structure in this paper. It can be seen from the figure that the DFT calculation results basically match the experimental values in this paper. Below room temperature, we only tested the low-temperature thermal conductivity in the b-axis. The DFT calculation results also is consistent with previous report[10]. In addition, the lattice constant changes greatly after 600 K as mentioned above, so the results of theoretical calculation deviate from the experimental value.

Reference

1. P. E. Blochl, *Phys Rev B*, 1994, **50**, 17953-17979.
2. G. Kresse and D. Joubert, *Phys Rev B*, 1999, **59**, 1758-1775.
3. G. Kresse and J. Furthmuller, *Phys Rev B*, 1996, **54**, 11169-11186.
4. J. P. Perdew, K. Burke and M. Ernzerhof, *Phys Rev Lett*, 1996, **77**, 3865-3868.
5. Togo and I. Tanaka, *Scripta Materialia*, 2015, **108**, 1-5.

6. Yamamoto, K. Ogawa and T. Takeuchi, *Mater Trans*, 2011, **52**, 1539-1545.

7. P. Wu, B. Zhang, K. Peng, M. Hagihala, Y. Ishikawa, M. Kofu, S. Lee, H. Kumigashira, C. Hu and Z. Qi, *Phys Rev B*, 2018, **98**, 094305.

8. W. Li, J. Hong, A. F. May, D. Bansal, S. Chi, T. Hong, G. Ehlers and O. Delaire, *Nat Phys*, 2015, **11**, 1063.

9. T. Dahal, Q. Jie, Y. C. Lan, C. F. Guo and Z. F. Ren, Phys Chem Chem Phys, 2014, **16,** 18170-18175.

10. R. Q. Guo, X. J. Wang, Y. Kuang, and B. L. Huang, *Phys Rev B*, 2015, **92**, 115202.